



ELSEVIER

Nuclear Instruments and Methods in Physics Research A 478 (2002) 511–526

**NUCLEAR
INSTRUMENTS
& METHODS
IN PHYSICS
RESEARCH**
Section A

www.elsevier.com/locate/nima

Design and commissioning of the GSI pion beam

J. Díaz^{a,*}, N. Yahlali^a, M. Ardid^a, M. Álvarez^a, V. Avdeichikov^d, H. Bokemeyer^b,
L. Carlén^d, B. Franczak^b, O. Hartmann^{c,b}, B. Jakobsson^d, W. Koenig^b,
U. Leinberger^b, B. Lommel^a, V. Metag^{b,c}, Yu.A. Murin^d, W. Mittig^c, W. Niebur^b,
R. Novotny^c, R. Schicker^b, R.S. Simon^b, A. Schröter^b, W. Schön^b

^a IFIC, Centro Mixto Universidad de Valencia-CSIC, Edificio Inst. de Investigacion, Apdo. de Correos 22085, E-46071 Valencia, Spain

^b Gesellschaft für Schwerionenforschung, D-64291 Darmstadt, Germany

^c II. Physikalisches Institut, Universität Gießen, D-35392 Gießen, Germany

^d University of Lund, SE-22100 Lund, Sweden

^e Grand Accélérateur National des Ions Lourds, F-14021 Caen, France

Received 18 January 2001; accepted 27 January 2001

Abstract

We describe the design of the secondary pion beam-line installed at the SIS 18Tm synchrotron at GSI, Darmstadt, and discuss the commissioning results. The experiments were performed with proton and ¹²C primary beams at several energies using beryllium production targets. Pion yields in a momentum range between 0.4 and 2.8 GeV/c were identified. At the highest primary beam energies of 3.5 GeV for proton and 2.0 A GeV for carbon ions, the latter beam produces the highest low-momentum pion yield while at momenta of 1.5 GeV/c the yields are comparable and at 2.8 GeV/c the proton beam is superior. A momentum resolution of around 0.5% is achieved and the time resolution (σ) ranges from 100 to 150 ps, for bombarding rates up to 1.5 MHz. © 2002 Elsevier Science B.V. All rights reserved.

PACS: 25.80.Ls; 29.70.Eg; 25.75.Dw; 29.27. – t

Keywords: Charged pion production; Pion beams; Secondary beams; Time-of-flight measurements

1. Introduction

A modification of hadron masses and their lifetimes in nuclear matter at normal density and zero temperature with respect to the values measured in vacuum has been predicted by recent theoretical calculations [1] to occur as a precursor phenomenon of the chiral symmetry restoration that should take place at high density and

temperature. These effects lack experimental evidence at present and their measurement is the main motivation for the installation of the GSI (Darmstadt) pion beam facility. The addition of a secondary pion beam to the already available proton and heavy ion beams will allow to study properties of hadrons with the same detector system at different nuclear matter densities produced by pion, proton and HI beams. The particular characteristics of the set of detector systems currently available or under construction at GSI, will make this facility unique. Many pos-

*Corresponding author. Fax: +34-963-864-581.

E-mail addresses: jose.diaz@ific.uv.es (J. Díaz).

sible experiments are foreseen where the already available detectors (TAPS [2], FOPI [3], KaoS [4], LAND [5]) will measure electromagnetic form factors and masses of baryons and mesons. These studies are essential for the understanding of the non-perturbative regime of Quantum Chromodynamics. The dilepton spectrometer HADES [6] in combination with the pion beam will allow to measure masses and widths of vector mesons produced at rest in nuclear matter by measuring their decay into electron–positron pairs. The GSI pion beam will constitute a general purpose facility.

The GSI pion beam is produced in the collision of a primary proton or heavy-ion beam from the SIS with a thick production target. Pions are transported to the experimental area through a beam-line in which a time-of-flight detector system composed of three hodoscopes is installed with the purpose of identifying pions and measuring their momenta. The commissioning experiment was carried out with primary beams of protons at 1.6 and 3.5 GeV and ^{12}C ions at 1.2, 1.7 and 2 A GeV incident energy. Beryllium production targets of 2, 4, 6 and 18.4 g/cm^2 were employed.

In the first part of this paper we describe the design and experimental setup of the pion beam-line. In the second part, we report on the design and general performance of the time-of-flight hodoscopes which are the main components of the pion beam factory besides the magnetic elements of the beam-line. In the last part, particle discrimination and produced pion rates are presented. It has been found as a by-product of the commissioning experiment, that electron and positron beams with sufficient intensity for calibration purposes can be produced. These leptonic beams will be useful for calibrating the HADES spectrometer. Preliminary accounts of the results presented in this paper have been given elsewhere [7].

2. Setup of the pion beam-line

2.1. Floor plan of the SIS target hall

The different beam-lines leading to the major experimental caves in the SIS target hall are shown

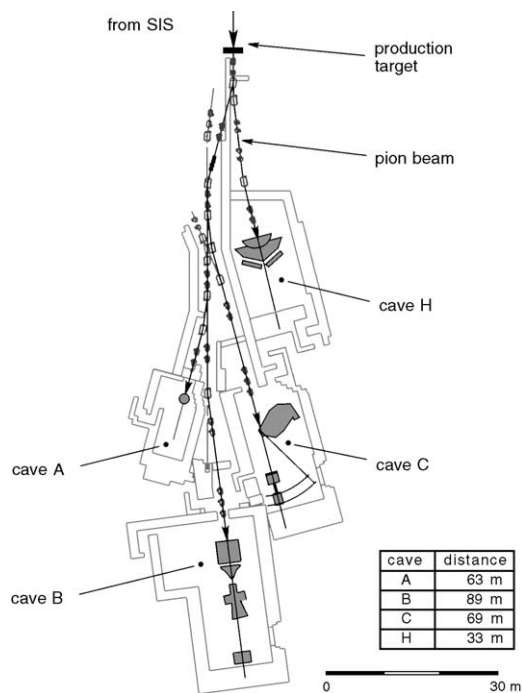


Fig. 1. Beam-lines in the SIS target hall.

in Fig. 1. The pion production target is located in the main beam-line coming from the synchrotron. The beam-line leading to cave H was chosen for the commissioning of the pion beam facility. This beam-line has 33 m length and is the shortest among the secondary beam-lines.

2.2. Production targets

A set of beryllium production targets of 2, 4, 6 and 18.4 g/cm^2 thickness was used during the commissioning experiment. This material was chosen according to previous experimental data and calculations in order to optimize the pion production intensities [19].

The 18.4 g/cm^2 target which has a length of 10 cm, a diameter of 7 mm and is pencil shaped along the last 3 cm, tapered to a final radius of 4 mm, was used as standard production target. The other three targets were installed for producing secondary nuclear beams by fragmentation. The production targets were fixed in a water-cooled copper block. Insertion or removal of any

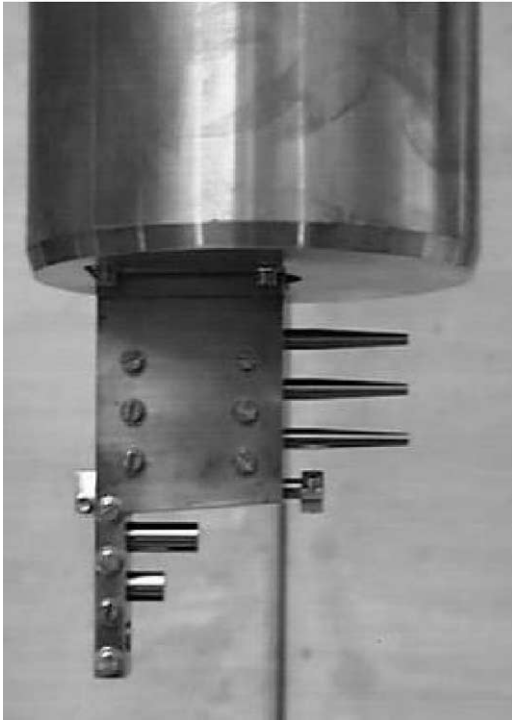


Fig. 2. Set of production targets fixed in their copper support. The three upper targets are 18.4 g/cm² thick and the targets below have a thickness of 6, 4 and 2 g/cm², respectively.

of the targets were controlled remotely from the SIS control room. A picture of the production targets installed in their support is presented in Fig. 2.

2.3. Pion beam-line optics

A schematic view of the beam-line leading to cave H, where the HADES detector is installed, is drawn in Fig. 3. The beam-line comprises two dipoles and 4 quadrupole doublets and has been designed for a momentum dispersion $\Delta x/(\Delta p/p)$ of -9 mm/%. The HADES target point is 70 cm higher than the pion production target. To transport the beam, the two dipoles had to be tilted slightly with respect to the horizontal plane in such a way that the first dipole introduces a vertical momentum component in the beam and the second dipole restores the momentum on the

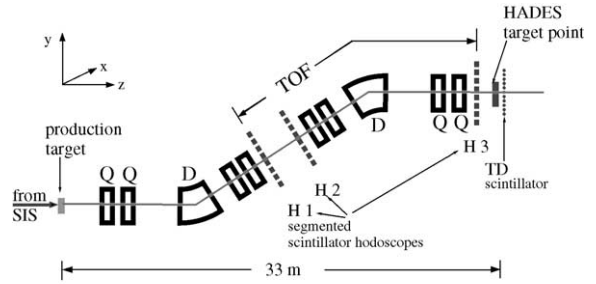


Fig. 3. Schematic drawing of the pion beam-line and its different elements.

horizontal plane. The beam-line has a momentum acceptance window of about 10% [8]. The $B\rho$ value of the beam-line can be chosen to select the central momentum of the acceptance window. In the experiment described in this paper, settings were selected to transport pions with momenta between 0.4 and 2.8 GeV/c.

3. The beam-line detectors

During the commissioning experiments three detector systems were installed along the pion beam-line: three segmented hodoscopes to track particle trajectories and provide time-of-flight measurements, a plastic scintillator at the HADES target position with the purpose of measuring the total number of particles crossing this point and a fiber scintillator array to determine the beam profile behind the HADES target position and the focal point of the beam.

3.1. The time-of-flight hodoscopes

The required momentum resolution for the various experiments is about $\Delta p/p = 0.5\%$ which is significantly higher than the 10% momentum acceptance of the beam-line. Therefore, an additional momentum measurement system was introduced based on tracking the pion trajectories.

Other particles produced along with the pions and having the same charge will be transported as well. Positive pion beams are contaminated with

positrons, positive muons, positive kaons, protons and nuclear fragments, while negative pion beams contain electrons, negative muons and kaons. In order to have a clean beam, pions have to be discriminated from the other particles. Time-of-flight measurements is one of the standard techniques employed for separating particles of different mass and this method is applied here.

Three segmented hodoscopes, indicated as H1, H2 and H3 in Fig. 3, were installed along the pion beam-line to achieve both momentum determination and mass separation. The first two hodoscopes H1 and H2 were placed between the second and third quadrupole doublet, as shown in Fig. 3. In this region the beam is dispersively defocused and distributed on a relatively large cross-section, which allows to keep the count rate of the individual hodoscope modules at acceptable values. In addition, this defocusing produces a useful correlation between the momentum and point of impact in the hodoscopes which can be exploited to determine the momentum of particles as described in Section 6. This correlation is illustrated in Fig. 4, where trajectories for particles incident in the beam direction with different momenta around the central momentum of the beam-line are drawn. The position of the third hodoscope, H3, was chosen such that the path for the time-of-flight with respect to both H1 and H2 is as long as possible.

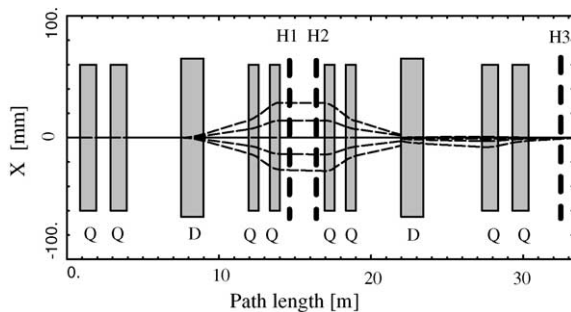


Fig. 4. Simulation of trajectories of pions emitted in the forward direction with different momenta. The central momentum is arbitrary. The continuous trajectory corresponds to central momentum and the dashed trajectories have been calculated for momenta of 2% and 4% above and below the central momentum. The shaded areas represent the corresponding quadrupoles and dipoles.

Previous simulations showed that a segmentation of the first two hodoscopes of 1 cm in the horizontal direction and a segmentation of the third hodoscope of 0.65 cm in the vertical direction would allow to obtain the required momentum resolution and to cope with the high count rate expected. Here, the count rate is kept below 10^6 counts/s per rod at the highest intensities of the primary beam. The first two hodoscopes are composed of 16 rods of BC404 plastic scintillator of 1 cm width, 0.5 cm thickness and 10 cm length, while the third hodoscope has 16 rods of 0.65 cm width, 0.65 cm thickness and 10 cm length. The scintillation light is read on both sides by Hamamatsu R3478 photomultiplier (PM) tubes which were selected for their excellent time resolution and small size. The scintillators were coupled to plexiglas light-guides glued to the PM tube windows. The light-guides of the first and second hodoscopes formed an angle of $\pm 13^\circ$ with the plastic scintillator in order to fit the PM tubes into the available space. The more compact design of the third hodoscope required to alternate modules with light-guides tilted an angle of $\pm 18^\circ$ with modules with straight light-guides. The scintillators and light-guides were wrapped with $40 \mu\text{m}$ aluminum plated mylar to make them light-tight. A technical drawing of the scintillator modules and their assembling is shown in Fig. 5.

In order to avoid a signal reduction associated to high count rates, active photomultiplier voltage divider chains were used. The chains are designed by SINKO (St. Petesbourg, Russia) closely following the emitter-follower scheme of Kim et al. [9,10].

The hodoscopes were housed in black metacrilate boxes as shown in Fig. 6. The boxes were screwed to the flanges of the beam-line pipe for high accuracy positioning. The connectors needed for scintillator signal cables and high-voltage cables were installed on the metacrilate boxes. The use of feed-through connectors, SHV for high voltage and LEMO for scintillating signals, facilitates the installation of the hodoscopes without an observable deterioration of the time profile of the scintillator signals.

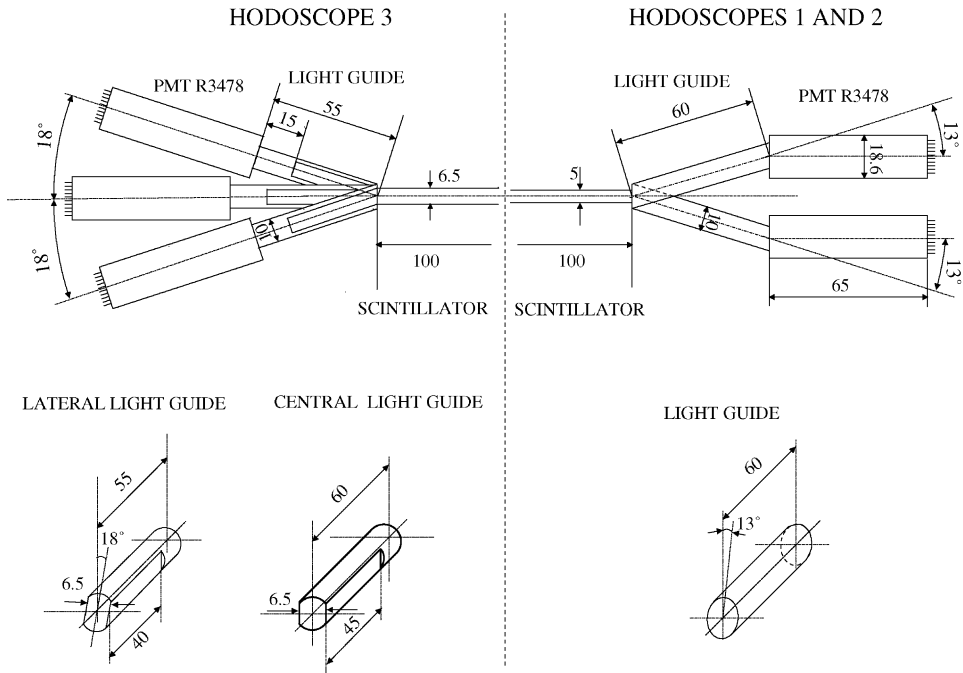


Fig. 5. Drawing of the scintillator modules of the first and second hodoscope (right) and third hodoscope (left). Only half of the modules are shown, the other half is symmetric. Detailed drawings of the corresponding light-guides are given as inserts in the bottom of the figure. Units are given in mm.

3.2. Laser monitoring

The hodoscopes were equipped with a laser source sending light pulses to each PM tube through quartz fibers with a three-fold purpose: to have a time reference, to monitor the electronics during the experiment and to correct in the off-line data analysis for drifts in the electronics. A N_2 pulsed laser of 3 mW power which radiates ultraviolet light (337 nm) was used. A trigger for laser events was implemented by means of a reference PM which was directly illuminated by the laser. The direct laser signal was fed into four 1 mm optical fibers which in their turn were split into bunches of 16 quartz fibers of 200 μm diameter. These fibers, previously polished to provide uniform splitting of light, were directly coupled to the windows of the PM tubes. The laser was operated at a frequency of 20 Hz during the experiment.

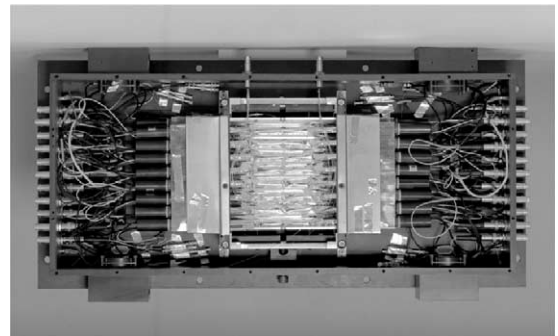


Fig. 6. Third hodoscope mounted inside its metacrilate housing.

3.3. Target detector

In order to determine the pion intensity at the HADES target position during the experiment a hexagonal ($\phi = 10\text{ cm}$) 1 cm thick plastic scintil-

lator read out by a Phillips XP2972 photomultiplier was installed. A dedicated trigger was implemented for this detector.

3.4. The scintillating fiber array detector

An array of 48 BCF92 Bicron scintillating fibers read out in groups of 16 by position-sensitive H6568 Hamamatsu photomultipliers was placed 2.85 m downstream of the third hodoscope. This detector was used to reconstruct the focus of the secondary beam and to provide an additional signal for the beam particles crossing the HADES target position. A sketch of this detector is shown in Fig. 7.

The scintillating fibers were coupled through optical fibers to the photomultipliers and were wrapped with 0.15 mm thick teflon foil in order to reduce light background and cross-talk. The surface of this detector is $6.4 \times 3.2 \text{ cm}^2$ and the spatial resolution is about 2 mm along the coordinate axes.

3.5. Electronics setup

The electronics setup consisted of a combination of VME and CAMAC modules. The electronic modules, apart from the VME crate, were placed in cave H. The VME crate was placed in the

counting room, separated from the CAMAC crates by about 90 ns of cable length. High-quality RG58 signal cables were used to transport the PM signals from the hodoscopes to the electronics; 22 and 10 m long cables were needed to transport the signals from the two first hodoscopes and from the third hodoscope, respectively. Each scintillating signal had to be split into three for timing, energy integration and triggering. The required timing accuracy of the order of 100 ps did not allow to perform active splitting of the signals. For this reason, the signals were fed directly into 8-channel CAMAC GSI 8001 constant fraction discriminators (CFD). These modules provide one OR output for the eight input channels, two differential ECL outputs per discriminated signal, and two additional analog outputs, operating as active splitters after discrimination. One of the analog outputs was used for energy integration. The OR output was used to make triggers for individual hodoscopes. The first of the logic outputs were sent as individual stop signals to the TDC modules. The second logic outputs were sent to the scalers that recorded individual channel rates. In order to reduce cross talk effects, the signal cables from the hodoscopes were connected to the CFD discriminators in such a way that neighbouring rods of the hodoscopes were never read into neighbouring CFD channels. Triggers were derived for the laser events, the target detector, the fiber array detector, and for each hodoscope. The triggers of individual hodoscopes consisted of the OR of the 32 hodoscope channels. The coincidence trigger was then produced as the AND of the three individual hodoscope triggers. A GSI TB8000 trigger box was used to implement the triggers. This module has the possibility of selecting suitable reduction factors for each individual trigger in order to adapt the rate of accepted events to the speed of the acquisition system. In addition, triggering was inhibited by the busy signal of the VME controller. Trigger signals that were neither inhibited nor scaled down were counted by scalers for an offline dead time correction. The Master Trigger output of the trigger box was used to build the Common Start signal for the Philips 7186H TDC modules and the gates for the Silena ADC 4418/Q charge

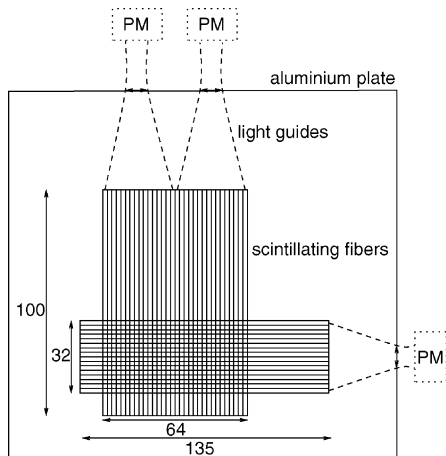


Fig. 7. Sketch of the scintillating fiber array. Dimensions are given in mm.

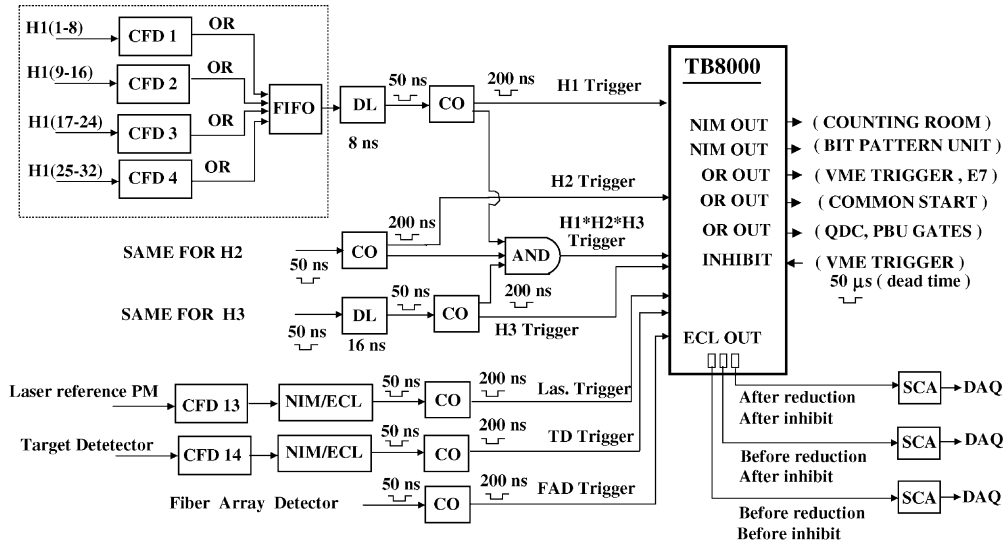


Fig. 8. Scheme of the electronics setup of the different triggers used.

integration modules. To postpone the arrival of the individual signals at the acquisition system, so that they come after the trigger signals, the TDC START and STOP logic signals were delayed by 500 ns using GSI DL1610 active delay modules which are designed for high accuracy timing.

Energy signals were delayed by means of cable delay. The overall loss in time resolution by the electronics is estimated to be around 50 ps. This should be compared to the total resolution of 110–150 ps presented in Section 5. The trigger scheme is shown in Fig. 8.

4. Data acquisition and data analysis

The experimental data were taken with the MBS [11] data acquisition system developed at GSI. The event structure contained the time and energy signals provided by each hodoscope scintillator, the energy signals of the target detector and fiber array detector, the trigger pattern and the scalers of all the CFD channels and triggers. The data acquired during the experiment were recorded on DLT magnetic tapes and analysed off-line with the help of the PAW [12] based code APE [13], which

decodes the raw events and stores the relevant data in PAW n-tuples.

5. Performance of the hodoscopes

The relevant features of the pion beam-line are the efficiency and maximum count rate that the hodoscopes accept and the time-of-flight and momentum resolution. In this section, we report on the behaviour of the hodoscopes at relatively high count rates, particularly the time-of-flight resolution. The mass resolution achieved at different momenta and the accuracy in the momentum reconstruction of the particles from the tracking information provided by the hodoscopes are discussed in Sections 7 and 8.

The performance of the hodoscopes at high count rates was studied in detail with the production target removed and the proton beam sent directly into the pion beam-line. The beam intensities varied between 10^4 particles/s and several times 10^6 particles/s. The primary beam intensity is not constant during the spill and this fact has been used to collect data at different bombarding rates.

At a count rate of about 3×10^6 particles/s a strong decrease in the amplitude of the PM signals was observed in a monitoring oscilloscope. The time-of-flight resolution (σ) between H1 and H3 or between H2 and H3 is around 100 ps up to a counting rate of about 10^6 particles/s, for the best rod combinations. At higher rates the time-of-flight resolution starts to get worse. At 2×10^6 particles/s the resolution is around 150 ps. The detailed analysis of these data is described in Ref. [10].

The trajectories of the particles are defined by the scintillators responding in each hodoscope. Time-of-flight spectra were obtained for each H1-H2-H3 trajectory. The trajectories with higher statistics were always those corresponding to equal or neighbouring rods in the two first hodosopes.

Two time signals were read out for each rod and the average of these signals was utilized to avoid position sensitivity in the time determination. The time calibration was performed with a time calibrator that produces a bunch of narrow pulses separated by 10 ns which are fed into the CFD channels. A linear behaviour was found over the full TDC's range. For each individual rod combination the time-of-flight spectrum was fitted by a Gaussian and this defined the peak position and the width (σ) of the distribution. Times are measured with respect to the COMMON STOP signal and therefore contain individual TDC offsets which were corrected for by requiring that the time-of-flight of pions of 2.5 GeV/c between the different rods in each hodoscope has the same value.

As an overall result we find that the time-of-flight resolution (σ) between hodoscopes H1 and H3 or H2 and H3 varies from 100 to 150 ps, with most of the rod combinations giving $\sigma < 120$ ps [10]. This is independent from the choice of beam or momentum setting of the beam-line. This resolution has contributions from the scintillators and PM tubes and from electronics. The time resolution of the electronics for individual channels (comprising both CFD and TDC modules) has been estimated from the width of the peaks produced by the time calibrator pulses. This was on average less than 50 ps, but with a wide distribution between 30 and 100 ps. The time

resolution of the scintillator modules deduced from these results varies between 70 and 100 ps.

The time peaks corresponding to laser events revealed the existence of a significant timing drift of the electronics over several hours. For recording during short times the drift was however well below 50 ps. The time-of-flight was corrected for drift by utilizing these laser events.

The efficiency of each hodoscope has been measured through the coincident events triggered by the target detector which have multiplicity at most one in each of the three hodoscopes (at most one scintillator in each hodoscope responds). These events correspond to particles that have passed through all three hodoscopes. The events with a multiplicity larger than one in any of the hodoscopes have been disregarded for this analysis. The hodoscope efficiency has been defined as the ratio between coincident events and events detected in the other two hodoscopes, for example, $\varepsilon_1 = H1 * H2 * H3 * TD / H2 * H3 * TD$ in the case of H1. These efficiencies, shown in Fig. 9 as a function of the beam momentum, are always close

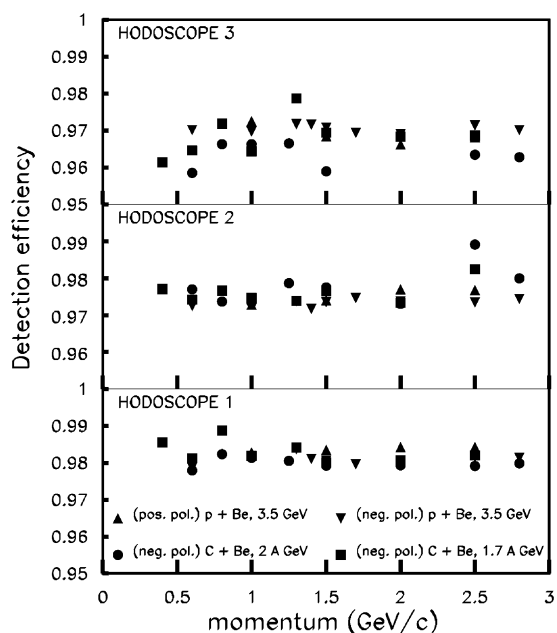


Fig. 9. Efficiency of the three hodoscopes for particles arriving to the target (multiplicity 1) versus central momentum for the different beams used in the experiment and for both polarities.

to 1. They characterize only the geometrical efficiency of the hodoscopes and the threshold setting quality and do not exhibit any significant variation with momentum.

According to simulations, the pion losses introduced by the hodoscopes are below 10% in the momentum range above 1 GeV/c [8].

6. Momentum calibration

The fact that the beam is defocused between the hodoscopes H1 and H2 and that the x -coordinates in the hodoscopes of particle trajectories depend strongly on the particle momentum, as illustrated in Fig. 4, has been used to obtain the momentum calibration. Varying the $B\rho$ setting of the beam-line for a beam of fixed momentum produces the same modification of particle trajectories as varying the momentum of the beam in the opposite sense with $B\rho$ fixed. This was used to obtain a relation between the momentum of the particles and the x -position of particle trajectories in the hodoscopes by removing the production target and letting a direct proton beam of 1.6 GeV incident energy into the pion beam-line. The $B\rho$ value was shifted by $\pm 2\%$, $\pm 5\%$, and 7% from the central value. In Fig. 10 (top panel) the correlation between the x -position in H1 and H2 hodoscopes for different $B\rho$ values is shown. The centroids of these distributions follow a straight line. In the middle panel of Fig. 10, the distribution of events is projected onto the $(x_1 + x_2)/2$ axis. As the momentum dispersion of the incident primary beam is negligible, the width of the $(x_1 + x_2)/2$ distributions is related to the momentum dispersion of particle trajectories. The widths of the projected distributions are slightly smaller than 0.4%, which gives an estimate of the momentum resolution of the pion beam-line. In the bottom panel of Fig. 10, the relative variation of momentum versus $(x_1 + x_2)/2$ is plotted. There is a linear correlation between these two quantities. This correlation has been exploited to obtain a momentum calibration from $(x_1 + x_2)$. Before entering a more detailed discussion of the momentum resolution of the beam-line we discuss the time-of-flight resolution and particle discrimination.

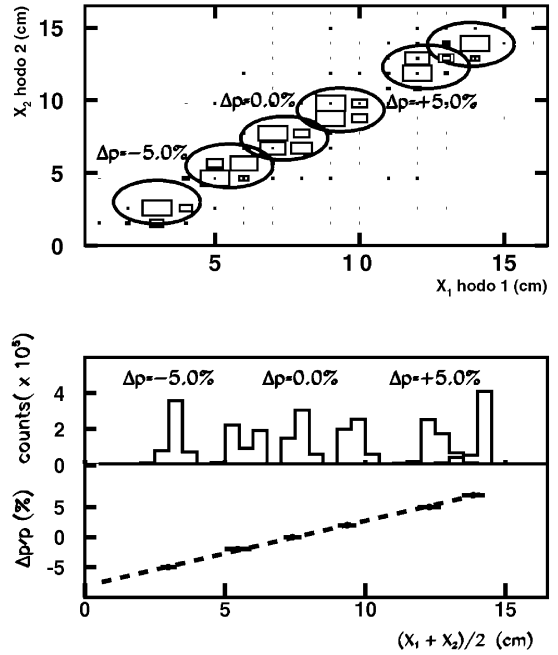


Fig. 10. Momentum calibration. In the upper picture, the bidimensional plot of the x coordinate in H2 versus the x coordinate in H1 for the six $B\rho$ settings measured is shown. In the central picture, the projection of the number of counts versus $(x_1 + x_2)/2$ is plotted. In the lower picture, the relative variation of momentum versus $(x_1 + x_2)/2$ is represented.

7. Particle discrimination

Particle masses can be calculated from time-of-flight measurements, provided the momentum is known, by the equation

$$mc^2 = \frac{pc}{l} \sqrt{(ct_f)^2 - l^2} \tag{1}$$

where l is the length of the trajectory between one of the first two hodoscopes and the third one, t_f is the corresponding time-of-flight, and p is the momentum of the particle. The most intense peaks observed in the mass spectra correspond to pions and protons for negative and positive polarities of the beam-line, respectively, for all the momentum settings measured. Electrons, positrons, charged pions of both signs, kaons, protons, and deuterons have been observed in

the time-of-flight spectra. Muons can be distinguished from pions only for the lowest $B\rho$ settings due to the finite time-of-flight resolution. In the following, we discuss the results obtained for different primary beams and beam-line polarities.

7.1. Results of measurements for a proton primary beam and positive polarity of the beam-line

Proton primary beams of 1.6 and 3.5 GeV incident energy impinged on the production target with the beam-line set to transport positive particles. For the 3.5 GeV primary beam, data were taken for central momenta of the beam-line between 1 and 2.5 GeV/c. For the 3.5 GeV primary beam, the relative intensity of pions, protons, and deuterons for different central momenta are given in Table 1. Positrons could be identified only at $p_0 = 1$ GeV/c.

In Fig. 11, time-of-flight spectra are shown for a proton primary beam at 3.5 GeV and for central momentum of the beam-line of 1 and 2.5 GeV/c, respectively. Peaks corresponding to pions, protons and deuterons are clearly seen. In the lower part of Fig. 11 the pion peak is displayed on a magnified scale showing a flat tail on the left side generated by positrons.

In Fig. 12, the mass spectra, calculated by Eq. (1) for the corresponding time-of-flight spectra of Fig. 11, are shown. At 1 GeV/c, apart from pions, protons, and deuterons two peaks corresponding to kaons and ^3He emerge. These peaks are not observable at 2.5 GeV/c within the available statistics.

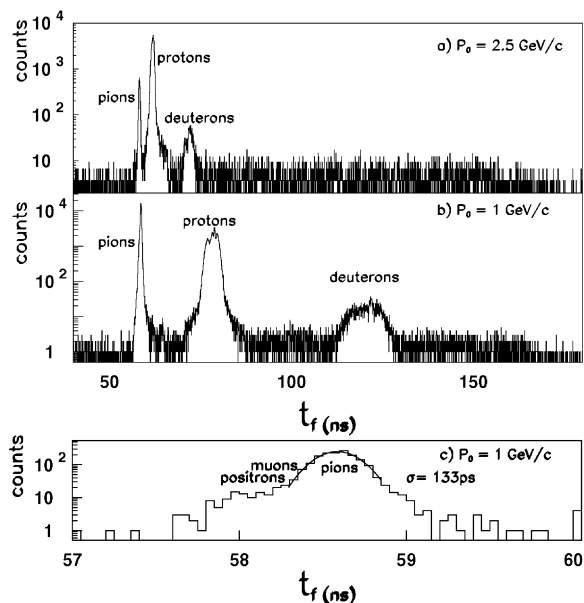


Fig. 11. Time-of-flight spectra for p at 3.5 GeV primary beam and for central momentum of the beam-line of 1 and 2.5 GeV/c and for positive polarity. Picture (c) shows a zoom of the pion peak for the 1 GeV/c case and for events hitting the rod 8 in the three hodoscopes. Positrons appear as a shoulder to the left of the pion peak.

7.2. Results of measurements for negative polarity of the beam-line

When the beam-line is set to negative polarity, electrons, muons, and negative pions are transported up to the HADES target position. Measurements were performed for primary proton beams of 1.6 and 3.5 GeV and for primary carbon beams of 1.2, 1.7, and 2.0 A GeV. The central

Table 1

Relative abundance of particles measured in the target detector for various central momenta of the positive polarity beam. Dashes (—) indicate that the corresponding particles could not be observed or resolved with the available statistics

Projectile	E (GeV)	p_0 (GeV/c)	e^+ (%)	π^+ (%)	K (%)	p (%)	$d + ^4\text{He}$ (%)	^3H (%)	^3He (%)
p	3.5	1.0	1.9	44.7	3×10^{-2}	50.3	1.3	0.1	5×10^{-2}
		1.5	—	42.8	5×10^{-2}	54.0	1.2	3×10^{-2}	2×10^{-2}
		2.0	—	13.7	6×10^{-2}	82.8	1.3	3×10^{-2}	—
		2.5	—	4.20	2×10^{-2}	90.9	1.0	2×10^{-2}	—

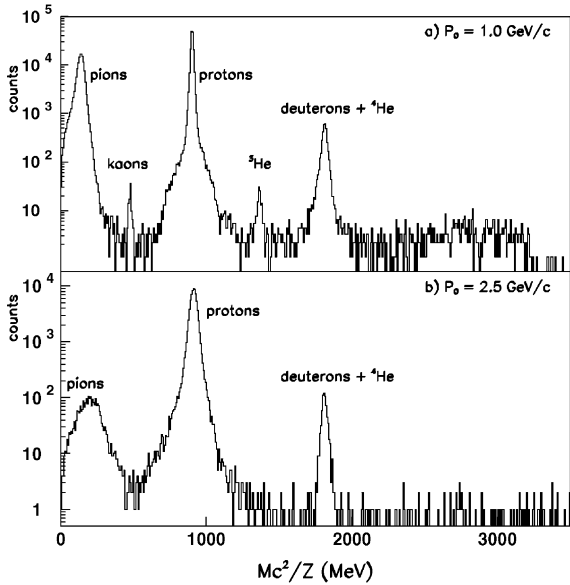


Fig. 12. Mass spectra of positive charged particles for the 3.5 GeV p primary beam and for central momenta of the beam-line of 1 and 2.5 GeV/ c .

Table 2

Relative abundance of pions and electrons at the HADES target position for different primary beams and central momenta, in the case of negative polarity of the beam-line

Projectile	Energy (A GeV)	P_0 (GeV/ c)	e^- (%)	π^- (%)
p	3.5	0.6	31.2	65.4
		1.0	12.4	87.0
		2.8	2.8	95.8
^{12}C	1.7	0.4	29.5	62.0
		0.6	8.5	88.6
		0.8	4.5	92.5
	2.0	0.6	9.8	85.1
		0.8	5.1	93.6
		1.0	2.8	95.8

momentum was varied between 0.4 and 2.8 GeV/ c . Muons could not be separated from pions. The relative intensities of electrons and negative pions are given in Table 2 for proton and ^{12}C primary beams.

In Fig. 13, the time-of-flight spectra of particles produced by a 2 A GeV ^{12}C and a 3.5 GeV proton primary beam are compared in the case of central

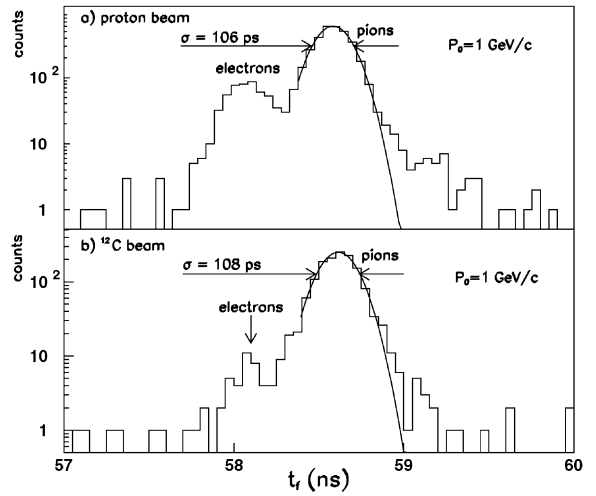


Fig. 13. Time-of-flight spectra of secondary particles for proton at 3.5 GeV and ^{12}C at 2 A GeV primary beams and for 1 GeV/ c central momentum of the beam-line, set to negative polarity.

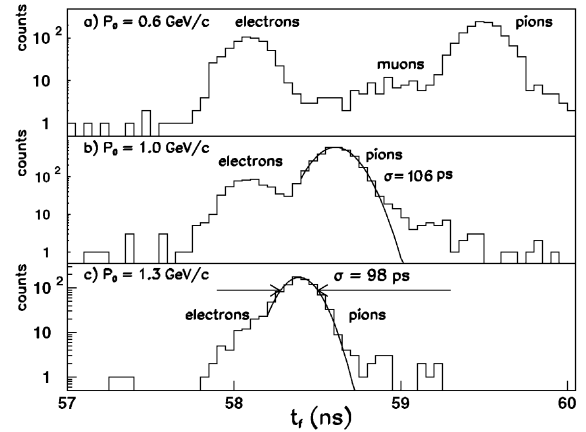


Fig. 14. Time-of-flight spectra of secondary electrons and pions for the 3.5 GeV proton primary beam and for central momenta of the beam-line of 0.6, 1 and 1.3 GeV/ c .

momentum of the beam-line of 1 GeV/ c . In Fig. 14, the time-of-flight separation of the electron and pion peaks is shown for a 3.5 GeV proton primary beam and for central momenta of the beam-line of 0.6, 1, and 1.3 GeV/ c , respectively. The indication of a muon peak at the momentum setting of 0.6 GeV/ c is not visible when going to higher beam-line momenta. The time-of-flight

spectra for 3.5 GeV proton and 1.7 and 2 A GeV/c carbon primary beams are compared in Fig. 15 for a central momentum of the beam-line of 0.6 GeV/c.

8. Momentum resolution

We showed in Section 6 that there is a linear correlation between the momentum of transported particles and the horizontal position ($x_1 + x_2$) of the particle trajectory in the two first hodoscopes. This correlation was found in the case of a direct primary beam with well-defined momentum. As the momentum resolution and momentum calibration are of crucial importance in determining the feasibility of a given experiment, it is necessary to check the momentum calibration procedure and to measure the momentum resolution also in the case of a secondary beam. With this purpose in mind, we have compared the momenta obtained from the calibration as a function of $x_1 + x_2$ to the momenta obtained directly from time-of-flight measurements. We present the results for the case of a secondary proton beam of 1 GeV/c central momentum. The primary proton beam and the outgoing protons produced by the re-scattering and reaction processes in the production target

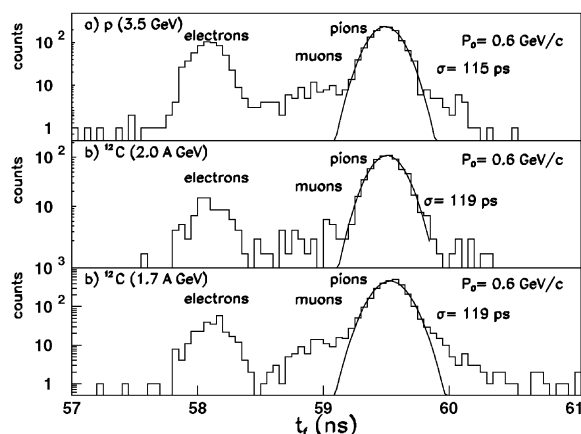


Fig. 15. Time-of-flight spectra of secondary electrons and pions for p at 3.5 GeV and ^{12}C of 1.7 and 2 GeV primary beams for 0.6 GeV/c central momentum of the beam-line.

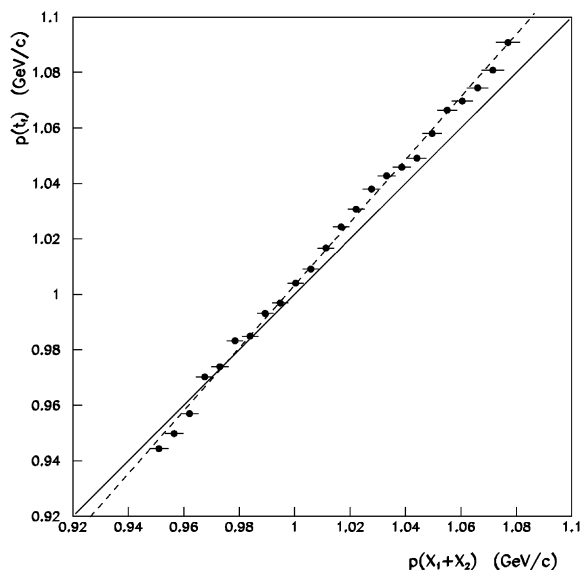


Fig. 16. Momentum from time-of-flight information versus momentum from impact position in the hodoscopes. The dashed line is a linear fit to the data and the solid line is a linear fit for vanishing coordinate in the origin. It is seen in the figure that the momentum resolution is of the order of 0.5%.

were transported along the beam-line. In Fig. 16, the momentum of the protons determined from the TOF is compared to the momentum set by the $x_1 + x_2$ scintillator rod position in the first two hodoscopes. The linear correlation is quite good, albeit with a slight deviation from unity slope as seen in Fig. 16. This discrepancy is probably due to the fact that the momentum from the TOF information is inaccurately calculated because the dependence of the exact path-length of the individual particle trajectories in the pion beam-line on momentum has been ignored in the present calculation. Calculations of this dependence by means of GEANT [14] simulations are in progress [8]. The deviation between time-of-flight and hodoscope coordinate momenta is however important only outside the central part of the acceptance window, where the number of transported pions is small. The momentum resolution is thus related to the fluctuations around the linear correlation of Fig. 16. It is found to be

within 0.5%, in agreement with the results presented in Section 6.

9. Pion intensity versus production target thickness

With the aim of determining the optimal design of the production target, the pion yield has been measured from four available production targets of thicknesses 2, 4, 6 and 18.4 g/cm². The pion intensity should have a maximum for the optimal target thickness and decrease for thicker targets due to the domination of pion absorption over pion production. The pion intensity is plotted versus the production target thickness in Fig. 17

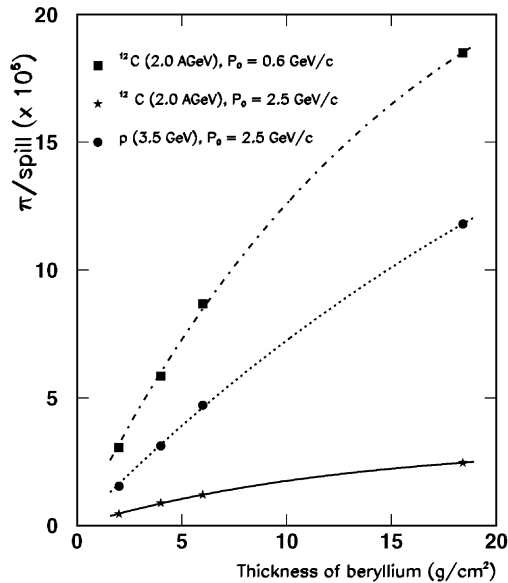


Fig. 17. Pion intensity in the target detector versus production target thickness.

for primary beams of 2 A GeV ¹²C and 3.5 GeV protons.

Numerous processes affect the final yield of pions from a thick Be target. The basic processes are of course pion production in p(¹²C) + Be reactions and pion absorption in the target nuclei. The production process is strongly energy dependent which is important here due to the energy degradation in the thick target. The absorption process has a strong pion energy dependence for low-energy pions. In addition, secondary projectile fragments from ¹²C also produce pions. This makes the quantitative optimal thickness prediction complicated.

In a simple model, the primary beam intensity I_P is attenuated by a thickness x of production target as $I_P(x) = I_P(0)\exp(-\Sigma_R x)$ where Σ_R is the macroscopic reaction cross-section of the primary beam in the production target, $\Sigma_R = \sigma_R \rho N_A / A$, where A and ρ are the atomic weight and density of the production target, σ_R is the reaction cross-section of the primary beam on the production target, and N_A is Avogadro's number. The pion intensity I_π is determined from the balance of pion production by the primary beam intensity I_P and pion absorption

$$\frac{dI_\pi}{dx} = \Sigma_p I_P - \Sigma_a I_\pi$$

which has the solution

$$I_\pi(x) = I_0(\exp(-\Sigma_R x) - \exp(-\Sigma_a x)) \quad (2)$$

where Σ_p and Σ_a are the macroscopical cross-section for pion production and absorption. This prescription thus accounts neither for energy loss and secondary production from fragments of the primary beam nor for scattering of pions in the production target and should be considered only

Table 3

Fitted parameters for the pion intensity in the HADES target position versus the production target thickness for p and ¹²C primary beams and for the pion momenta given in the third column

Projectile	E_0 (A GeV)	p_0 (A GeV)/c	I_0 $10^5 \pi/\text{spill}$	Σ_R $10^{-3} \text{cm}^2/\text{g}$	Σ_a $10^{-3} \text{cm}^2/\text{g}$
p	3.5	2.5	120 ± 10	(11 ± 1)	(18 ± 1)
¹² C	2	2.5	82 ± 6	(32 ± 1)	(35 ± 1)
¹² C	2	0.6	238 ± 10	(24 ± 1)	(31 ± 1)

as a crude approximation. The curves in Fig. 17 are fits of double exponential functions as given in Eq. (2), with Σ_R , Σ_a and I_0 as free parameters. The results of these fits are presented in Table 3. The fitted parameters are in agreement with the reaction cross-sections of protons and carbon on beryllium (268 ± 6 and 806 ± 9 mb, respectively [15,16]), and with empirical knowledge about pion production and absorption [17]. However, the double exponential function is not sufficient to estimate the optimal target thickness for pion production. Fig. 17 shows that with 18.4 g/cm^2 the optimal target thickness with respect to the total yield has not been reached. The optimal thickness must be chosen as a compromise between production yield and the background rate, especially for positive particles. For the experimental application thicker production targets are currently under investigation.

10. Background rate

Events with a multiplicity larger than 1 or events missing information in a hodoscope have been considered as background. In an attempt to quantify the background of a given hodoscope, it has been defined as the relative difference between the total number of events in the hodoscope and the number of coincident events with multiplicity 1 in the three hodoscopes. These numbers of events have been derived from the information provided by the scalers which are not inhibited by dead time. For hodoscopes H1, H2 and H3, the background ratio varies between 85% and 99.4%, between 74% and 98%, and between 2.8% and 5.4%, respectively, depending on the primary beam and central momentum settings.

11. Intensity of pions and electrons at the target position

The maximum achievable pion rate at the HADES target position is the main information to be extracted from this commissioning experi-

ment. This experiment was carried out at intensities much lower than maximally possible which is determined by the space-charge limit of the SIS primary beam. To calculate the highest intensities we have measured the coincident events in the three hodoscopes as a function of the intensity of particles extracted from SIS. The extraction efficiency from SIS was measured before every run with the help of ionization chambers placed along the beam-line preceding the production target and it was always found to be between 73% and 75%. The focusing of the beam-line was optimized before the runs by performing a fine tuning of the currents in quadrupoles and steerers in order to get the maximum intensity in the target detector. The intensity of coincident pions in the three hodoscopes is given in Fig. 18 (points) as a function of the central momentum of the beam-line, for p and ^{12}C primary beams of the maximum intensity that can be extracted from SIS. These

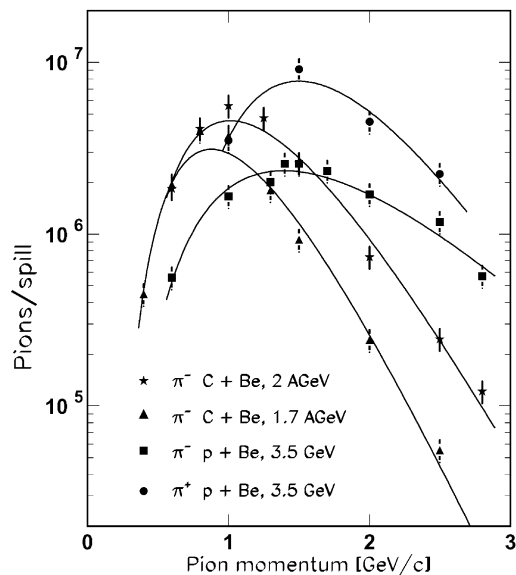


Fig. 18. Pion intensity in the target detector for p and ^{12}C primary beams at different energies as a function of the central momentum of the beam-line. The primary beam intensities correspond to the maximum intensity to be extracted from SIS, i.e. 1.7×10^{11} protons/spill and 5×10^{11} carbon ions/spill, respectively. The solid curves represent fits to the data using Eq. (4) as explained in the text. The fit parameters are given in Table 4.

intensities are 1.7×10^{11} and 5×10^{11} particles/spill for proton and carbon beams, respectively. It is observed that at low pion momenta the carbon beam produces higher pion intensities, at about 1.5 GeV/c the pion intensities are comparable and at the highest pion momenta proton beams are more effective.

The production cross-sections can be understood with the assumption that the pion energy satisfies a Boltzmann distribution in the nucleon–nucleon center of mass [18]

$$\frac{d^3\sigma_{cm}^\pi}{p_{cm}^2 dp_{cm} d\Omega_{cm}} = K \exp\left(-\frac{E_{cm}}{T}\right) \quad (3)$$

where the inverse slope parameter T is normally identified as a temperature. Boosting this distribution to the laboratory system and correcting for pion decay along the pion beam-line, we obtain for the pion production cross-section the equation

$$\begin{aligned} \frac{d^3\sigma_{lab}^\pi}{dp_{lab} d\Omega_{lab}} &= K p_{lab}^2 \frac{\gamma_{NN}(E_{lab} - \beta_{NN} p_{lab})}{E_{lab}} \\ &\times \exp(-\alpha/p) \exp\left(-\frac{l}{\beta_\pi c \gamma_\pi \tau_\pi}\right) \\ &\times \exp\left(-\frac{\gamma_{NN}(E_{lab} - \beta_{NN} p_{lab})}{T}\right) \end{aligned} \quad (4)$$

where p_{lab} is the pion momentum in the laboratory system, $E_{lab} = \sqrt{p_{lab}^2 + m_\pi^2}$, l is the length of the pion trajectory in the beam-line, $\beta_{NN}c$ is the nucleon–nucleon center of mass velocity, $\gamma_{NN} = 1/\sqrt{1 - \beta_{NN}^2}$, $\beta_\pi c$ is the pion velocity, $\gamma_\pi = 1/\sqrt{1 - \beta_\pi^2}$ and τ_π is the pion life-time in the rest system. A phenomenological absorption factor $\exp(-\alpha/p)$ is introduced to account for losses in the production target. Fitting the data with Eq. (4) yields the solid curves shown in Fig. 18 and the parameters listed in Table 4.

An important collateral result of this experiment is that the intensity of the electron component of the secondary beam will be sufficient for detector tests and calibration purposes. This intensity, extrapolated to the maximum intensity of SIS stated above, is plotted in Fig. 19 for the different primary beams. The origin of these electrons is mainly the external conversion of gamma-rays

Table 4

Parameters of Eq. (4), obtained by fitting the pion intensities in the target detector versus pion momentum for p and ^{12}C primary beams

Projectile	E_0 (A GeV)	Polarity	T MeV	α GeV/c
p	3.5	+	120	4.97
p	3.5	–	160	1.15
^{12}C	1.7	–	106	1.25
^{12}C	2	–	107	1.46

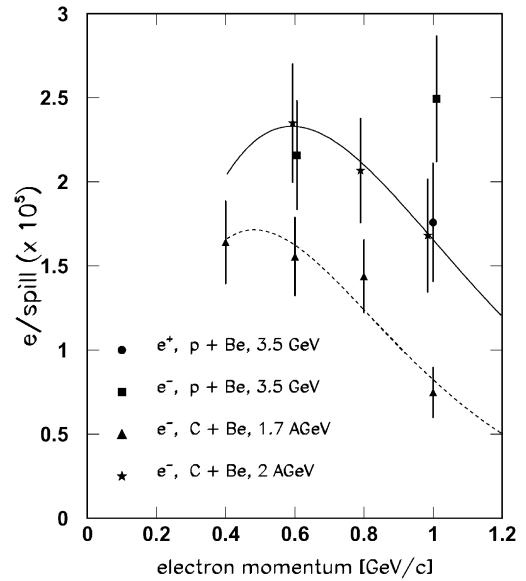


Fig. 19. Intensity of electrons in the target detector for p and ^{12}C primary beams at the different measured energies as a function of the central momentum of the beam-line. The solid and dashed curves are fits of Eq. (4) to the 2 and 1.7 A GeV carbon primary beam data, respectively.

produced in π^0 decay and to a lesser extent Dalitz decay. In future experiments, a Cherenkov detector will be installed to measure the electron intensity in the momentum range above 1 GeV/c. Temperatures of 98 and 116 MeV are obtained for carbon primary beams at 1.7 and 2 A GeV incident energies, respectively, when fitting the electron intensities as a function of the momentum by Eq. (4) without the decay factor.

12. Conclusions

In this paper, the GSI pion beam facility has been presented which has recently become available. The design of the pion beam-line and the hodoscopes, which measure time-of-flight and momentum, has been discussed. The different detector elements placed in the pion beam-line and the electronics of the commissioning experiment have been described. The time-of-flight and momentum resolution of the hodoscopes have been measured and found to be in agreement with the initial requirements. Finally, the expected pion intensities for the maximum primary beam intensity that can be extracted from SIS are presented. As a main conclusion, the 3.5 GeV proton primary beam gives higher pion yields than the 2 A GeV carbon primary beam for pion momenta larger than 1.5 GeV/ c and becomes about one order of magnitude larger at 2.8 GeV/ c . However, for pion momenta below 1.5 GeV/ c the use of a carbon primary beam is more favorable. The π -beam intensity is sufficient to allow a broad physics program in conjunction with the different detector systems available at GSI, in particular, the HADES spectrometer. In addition, it has been found that an electron component of sufficient intensity for detector test and calibration measurements is present in the secondary beam.

Acknowledgements

This work has been supported in part by the EC under contract FMGE-CT95-0009, by GSI and by the spanish DGICYT under contract PB95-1114-C02-01. M. Ardid acknowledges Generalitat Valenciana for a Ph.D. grant.

References

- [1] R. Rapp, J. Wambach, Chiral symmetry restoration and dileptons in relativistic heavy-ion collisions, preprint hep-ph/9909229, 1999.
- [2] R. Novotny et al., IEEE Trans. Nucl. Sci. NS-38 (1991) 379; A. Marín et al., Phys. Lett. B 409 (1997) 77; A. Marín et al., Nucl. Instr. and Meth. A 417 (1998) 137.
- [3] A. Gobbi, et al., Nucl. Instr. and Meth. A 324 (1993) 156; D. Pelte et al., Z. Phys. A 359 (1997) 55.
- [4] P. Senger, et al., Nucl. Instr. and Meth. A 327 (1993) 393; C. Müntz et al., Z. Phys. A 352 (1995) 175.
- [5] T. Blaich, et al., Nucl. Instr. and Meth. A 314 (1992) 136.
- [6] R. Schicker, et al., Nucl. Instr. and Meth. A 380 (1996) 586.
- [7] R.S. Simon, Prog. Part. Nucl. Phys. 42 (1999) 247; N. Yahlali, M. Ardid, J. Díaz, M. Álvarez, Czech. J. Phys 50/S2 (2000) 140; M. Ardid, N. Yahlali, J. Díaz, M. Álvarez, in: B. Rubio, M. Lozano, W. Gelletly (Eds.), Experimental Nuclear Physics in Europe, American Institute of Physics, New York, 1999.
- [8] M. Álvarez, et al., in preparation.
- [9] Y.D. Kim, et al., Nucl. Instr. and Meth. A 372 (1996) 431.
- [10] Yu. Murin, et al., LUND Preprint, LUIP 0001 (2000), Nucl. Instr. and Meth. A, to be submitted.
- [11] R. Barth, et al., MBS, GSI Multi-Branch System User Manual, GSI Report, 1997.
- [12] R. Brun, O. Couet, C. Vandoni, P. Zananini, PAW-Physics Analysis Workstation, CERN Program Library entry Q121, 1995.
- [13] M. Samek, APE-Analysis in PAW Environment, CERN Computer Newsletter 208 (1992) 14; M. Samek, M. Dahlinger, Version 2.2, GSI Report, 1995.
- [14] GEANT 3.21, CERN program library W5013, CERN Geneva.
- [15] D.E. Groom, et al., Eur. Phys. J. C15 (2000) 1; P.V.R. Murthy, C.A. Ayre, H.R. Gustafson, L.W. Jones, M.J. Longo, Nucl. Phys. B 92 (1975) 269.
- [16] I. Tanihata, et al., Phys. Rev. Lett. 55 (1985) 2676.
- [17] A.S. Clough et al., Nucl. Phys. B76 (1974) 15; V.V. Gachurin et al., Preprint ITEP-85-59, 1985.
- [18] R. Averbek, et al., Z. Phys. A 359 (1997) 65.
- [19] B. Lommel, Status report on the pion production target, GSI Annual Progress Report, 1997.